ACS OMEGA

http://pubs.acs.org/journal/acsodf

Article

Experimental Study on Bubble Dynamics and Mass Transfer Characteristics of Coaxial Bubbles in Petroleum-Based Liquids

Li Mei, Xiaopeng Chen, Bei Liu, Zhongyao Zhang, Tingting Hu, Jiezhen Liang, Xiaojie Wei, and Linlin Wang*

Cite This: *ACS Omega* 2023, 8, 17159−17170

Read Online

ACCESS | Metrics & More | Article Recommendations

ABSTRACT: Petroleum-based liquids are from an important petroleum-based polymer, whose application and preparation involve multiple operations related to gas−liquid two-phase flow. Due to insufficient research on gas−liquid two-phase flow, there is a gap in bubble dynamics and mass transfer characteristics in petroleum-based liquids. Accordingly, we have systematically investigated the bubble formation process, bubble rising dynamics, and mass transfer of coaxial bubbles. Herein, the contour of bubbles was obtained for analyzing the bubble formation process. It was found that the increase of gas flow rate contributed to the increase of bubble generation size, while the liquid viscosity had an inhibitory influence on the increase of bubble generation size. Moreover, the variation of bubble rising velocity was considered and the force analysis of the rising bubble was provided. A new model of drag coefficient applicable to petroleum-based liquids was proposed. Finally, variations in the amount of dissolved oxygen in the liquid were measured to analyze the mass transfer characteristics. The increase in nozzle inner diameter and gas flow rate both promoted mass transfer, but the increased liquid viscosity hindered mass transfer.

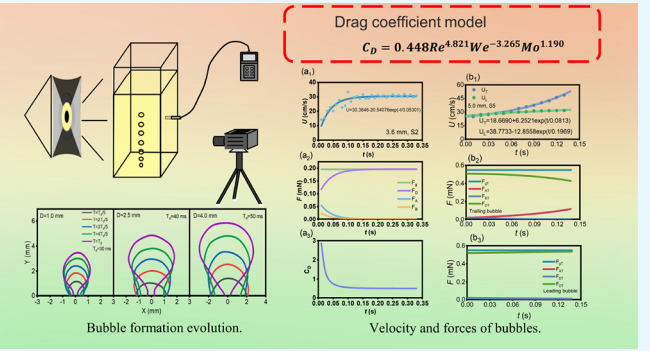

1. INTRODUCTION

Petroleum-based polymers including polyacrylamide, dicyclopentadiene, and petroleum resin are commonly used in diverse essential products to meet the basic human needs.[1] The petroleum resin is an essential petroleum-based polymer produced by the polymerization of C9 aromatic fraction, which has the advantages of acid and alkali corrosion resistance, excellent water resistance, light aging resistance, miscibility, adhesion, and low production cost.[2,3] It is widely used in many industrial fields such as waterproofing agents, high-end inks, adhesives, and rubber additives.[4,5] In industry, petroleum resin is dissolved in the organic solvent cyclohexane and is prepared as a petroleum-based liquid.[6] As a result, the various applications and preparations of petroleum resin involve numerous operations related to gas−liquid two-phase flow, e.g., the vapor stripping and distillation processes of polymerization to prepare petroleum resin, the foaming process of petroleum resin used to produce flame retardants, and the hydrogenation modification process of petroleum resin.[7,8] In these operations, the gas is shown as bubbles in the liquid with complex behaviors and the bubbles often appear as bubble swarms in the gas−liquid contactors. The bubbly flows act as a vital role in the mixing and mass transfer between gas and liquid. Coaxial bubbles, as a part of the bubble motion studies, are the basis and prerequisite for the investigation of bubble swarms.[9] Moreover, knowledge of the coaxial bubbles dynamics and mass transfer characteristics benefits the advance optimal design and operation of industrial unit used for petroleum-based polymers.

In the past decades, numerous efforts on bubble formation, bubble rising dynamics, and mass transfer in water or water-based solutions have been published. Mohseni et al.[10] examined the bubble formation in air and deionized water systems and analyzed the growth of various forces imposed on the bubble surface in the process of bubble formation. They revealed that the formation of bubbles at a submillimeter orifice cannot be depicted by quasi-static force balance. Wang et al.[11] investigated bubble formation behaviors in water under constant flow conditions and established a model for the forces during bubble formation. In terms of the bubble rising motion, Xiang et al.[12] explored the rising bubble characteristics in water

Received: March 6, 2023
Accepted: April 24, 2023
Published: May 4, 2023

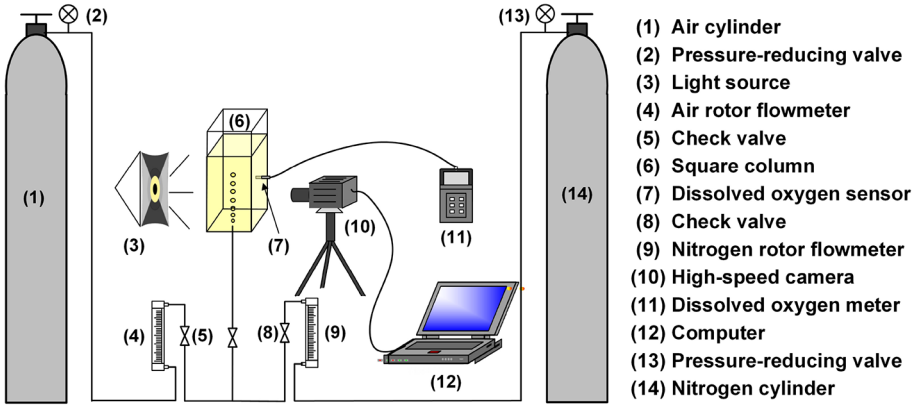

Figure 1. Schematic diagram of the experimental setup.

and introduced the force balance equation considering the additional mass effect. Oshaghi et al.[13] conducted an experimental study on the bubble rising behavior in aqueous solutions of glycerol and carboxymethylcellulose to analyze the bubble velocity. Gómez-Díaz et al.[14] analyzed the impact of liquid viscosity on the volumetric mass transfer coefficient using pure carbon dioxide as the gas phase and different concentrations of carrageenan aqueous solution as the liquid absorption phase. Shi et al.[15] examined the influence of orifice diameter and superficial gas velocity on bubble dynamics and mass transfer in NaOH aqueous solutions. Different literature sources presented the drag model of the bubble in experiments calculated with the Reynolds number (Re), Weber number (We), and Morton number (Mo).[16−20] They are defined respectively as

$$Re = \frac{\rho_l d_e U}{\mu_l} \tag{1}$$

$$We = \frac{\rho_l d_e U^2}{\sigma} \tag{2}$$

$$Mo = \frac{g\mu_l^4(\rho_l - \rho_g)}{\rho_l^2 \sigma^3} \tag{3}$$

in which ρ_l and ρ_g are the density of liquid and gas, respectively; μ_l and σ are the liquid viscosity and the liquid surface tension, respectively; U is the bubble velocity; and d_e is the bubble equivalent diameter. Cai et al.[21] investigated with deionized water and glycerol aqueous solution as liquid and improved and extended the work of Jamialahmadi et al.[22] They obtained a new drag coefficient model that is applicable to a broad range of system properties. Sun et al.[23] experimented with different aqueous solutions (sodium chloride solution, xanthan gum solution, and sodium dodecyl benzene sulfonate solution) and developed a model for the drag coefficient of rising air bubbles in a quiescent liquid.

In summary, bubble dynamics and mass transfer characteristics in water or water-based solutions have been well studied and reported, but research on petroleum-based solutions is still insufficient. It is known that in water-based systems, the liquid viscosity and surface tension have an impact on the bubble dynamics and mass transfer characteristics.[24−26] Compared to the water-based solutions, the petroleum-based liquids have lower surface tensions and higher viscosities. Chaumat et al.[27] compared the motion of bubbles in cyclohexane and water and found that they were significantly different. Mehrnia et al.[28] made a comparison of kerosene, diesel, and distilled water. They discovered that in kerosene and diesel systems, the values of gas hold-up and volumetric oxygen mass transfer coefficients were in majority instances quite higher than the water systems. Hence, the phenomenon of bubble dynamics and mass transfer characteristics should be different for water-based solutions and petroleum-based solutions.

In this paper, we report on bubble dynamics and mass transfer characteristics of coaxial bubbles in petroleum-based liquids. Different concentrations of cyclohexane petroleum resin solutions and air were selected as the study subjects. The bubbly flow regimes were discussed, and the contour of bubbles was obtained for analyzing the bubble formation process. The change of bubble rising velocity was considered, and the force analysis of the rising bubble was carried out. A new drag coefficient model suitable for petroleum-based liquids was proposed and compared with experiments. Moreover, the effect of bubble behavior on mass transfer was examined.

2. EXPERIMENTAL SECTION

2.1. Materials. The C9 petroleum resin (Gardner color grade no. 11, bromine value of 30.1 g/100 g) was purchased from PetroChina Lanzhou Huifeng Petrochemical Co., Ltd. (Lanzhou, China). The cyclohexane (C_6H_{12}, analytical reagent) was supplied by Guangdong Guanghua Sci-Tech Co., Ltd. (Guangdong, China). The air and nitrogen (>99.99%) were provided by Nanning Air Separation Gas Co., Ltd. (Nanning, China).

2.2. Experimental Setup. The experimental setup is schematically displayed in Figure 1. The experiments were conducted in a square tank, which was made of transparent acrylic. Different concentrations of cyclohexane petroleum resin solutions (CPRS) were selected as the liquid phase, and air and nitrogen were selected as the gas phase. Pure cyclohexane solution was S1, and the mass fractions of 5, 15, 25, and 35% of CPRS were S2, S3, S4, and S5, respectively. A stainless-steel nozzle was installed at the square tank's bottom center to generate bubbles. Nozzles with inner diameters (D) of 1.0, 2.5, and 4.0 mm were selected for this experiment. Check valves were placed strategically in the pipeline connected to the nozzle to avoid any backflow. The experimental gases (air and nitrogen) were supplied by the corresponding gas cylinders and reached the nozzle through the pressure-reducing valve, rotor flowmeter, and check valve

https://doi.org/10.1021/acsomega.3c01526
ACS Omega 2023, 8, 17159−17170

to form bubbles released into the square tank. The gas flow rate was adjusted to the desired value by the rotor flowmeter. These experiments were conducted at ambient temperature (25 °C) and under atmospheric pressure.

The liquid density and viscosity were measured using a petroleum densitometer (BF-18) and a rotational viscometer (NDJ-79), respectively. The liquid surface tension was tested with a surface tension meter (JZY-180). The fundamental physical parameters of the liquid in this experiment are shown in Table 1.

Table 1. Physical Properties of the Liquids in This Experiment

	mass fraction (wt %)	density, ρ (kg/m^3)	viscosity, μ (Pa·s)	surface tension, σ (N/m)	Morton number
S1	0	779.0	0.0014	0.0254	2.94E-09
S2	5	785.5	0.0016	0.0264	4.42E-09
S3	15	805.5	0.0018	0.0255	7.67E-09
S4	25	834.0	0.0036	0.0264	1.07E-07
S5	35	859.5	0.0092	0.0311	2.83E-06

The square tank with dimensions of 250 × 250 × 400 mm was used in these experiments. At the beginning of the experiment, the liquid was filled into the square tank and it was kept at 300 mm above the top edge of the nozzle. The bubble images were photographed by a high-speed camera (Revealer High Speed Camera, 2F01). The high-speed camera was located in front of the square tank and was connected to a computer. Its frame rate was set to 500 fps. Images were taken by one lens (Tamron, AF17−50 mm, F/2.8, and ø67 mm, A16) with a resolution of 520 × 800 pixels. The photographic illumination was supplied by an LED lamp (EF-200), which was located at the back of the square tank. The square diffusion fabric between the square tank and the LED light was utilized as a light diffuser to distribute the light evenly.

After the bubble images were photographed by the high-speed camera, they were processed by a set of self-programming programs to obtain rising bubble information, such as velocity, size, and shape. Figure 2 shows the typical images during the image processing. First, the bubble image background was removed using the subtraction of images in digital image processing techniques; the processed image is presented in Figure 2b. Next, the noise in the image was processed with wavelet filtering and image binarization methods, and the bubble contour was obtained by the Canny algorithm. The bubble contour is obtained as illustrated in Figure 2c. Finally, the bubble was filled, as shown in Figure 2d. However, not only a single bubble but also connected bubbles were involved in this experiment. If it is a single bubble, its bubble information can be extracted directly; if it is a pair of connected bubbles, they need to be segmented by the watershed segmentation method before extracting the bubble information.[29]

2.3. Bubble Size, Shape, and Velocity Measurements. The bubble area (A) was determined by calculating the filled area pixels. The bubble equivalent diameter (d_e) was derived from the bubble area, which was the same as that of a circle with the equivalent area. It is obtained by the following equation:

$$d_e = \sqrt{\frac{4A}{\pi}} \tag{4}$$

The bubble centroid coordinate was calculated by averaging all pixels in the bubble.

$$X_i = \sum_{i,j\in\Omega} i/N \tag{5}$$

$$Y_i = \sum_{i,j\in\Omega} j/N \tag{6}$$

Here, X_i represents the horizontal coordinates of the bubble centroid; Y_i represents the vertical coordinates of the bubble centroid; i is the horizontal coordinate of each pixel in the bubble area; j is the vertical coordinate of each pixel in the bubble region; N is the sum count of pixels in the region enclosed by the bubble boundary, and Ω is the set of pixels.

The bubble velocity was calculated from the coordinates (X_i, Y_i) of the bubble centroid. Each bubble horizontal velocity (V_x) and vertical velocity (V_y) were calculated according to the following equations.

$$\text{horizontal velocity } V_x = \frac{X_{i+1} - X_i}{\Delta t} \tag{7}$$

$$\text{vertical velocity } V_y = \frac{Y_{i+1} - Y_i}{\Delta t} \tag{8}$$

$$\text{instantaneous velocity } U = \sqrt{V_x^2 + V_y^2} \tag{9}$$

where (X_{i+1}, Y_{i+1}) and (X_i, Y_i) denote the center coordinates of the bubble in two continuous images and Δt is the time difference between two consecutive images.

2.4. Mass Transfer Measurement. In this experiment, the gas−liquid mass transfer coefficient was obtained by the dynamic oxygen absorption method. The square tank with length, width, and height of 100, 100, and 300 mm was used. 2.5 L of liquid was poured into the square tank in the experiment. The bubble size was obtained by using the high-speed camera. The dissolved oxygen concentration (DOC) was continuously monitored and recorded using a dissolved oxygen meter (Tengine Innovation, PDO1000) with the oxygen sensor. The oxygen sensor tip was coated with a fluorescent material that emits red light (RL) when modulated blue light (BL) shone on the fluorescent substance and was excited. As a reference, a red-light source (RLS), which was

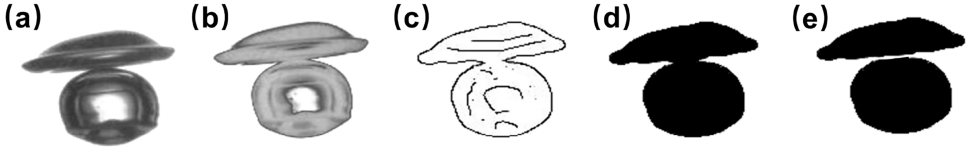

Figure 2. Bubble image processing process: (a) the original image; (b) background-removed image; (c) edge-extracted image; (d) the filled image; (e) the image after bubble segmentation.

https://doi.org/10.1021/acsomega.3c01526
ACS Omega 2023, 8, 17159−17170

synchronized with BL, was used. It measured the phase difference between RL and RLS and compared it with the internal calibration value. After linearization and temperature compensation, the concentration of oxygen was calculated. Calibration of the dissolved oxygen meter was done with anaerobic water. The oxygen sensor was placed 160 mm above the bottom of the square tank.

Dissolved oxygen in the liquid was purged by continuously injecting nitrogen into it. When DOC in the liquid was below 0.2 mg/L, it was considered that the oxygen in the liquid was almost completely purged and the nitrogen flow was stopped. Then, air was injected into the liquid and DOC was continuously monitored using the oxygen sensor until it reached a saturated steady-state value. Assume that the gas–liquid system is perfectly mixed and the variation of oxygen concentration in the bubbles is negligible. The oxygen volume mass transfer coefficient (k_La) of the square tank is obtained using the following equation:[30,31]

$$\ln\left(\frac{C_L^* - C_L}{C_L^* - C_0}\right) = -k_L a t \tag{10}$$

in which C_L* is the liquid's oxygen saturation concentration, C_L is the liquid's current oxygen concentration, and C_0 is the liquid's initial oxygen concentration. A straight line is obtained with time (t) as the horizontal coordinate and $\ln((C_L^* - C_L)/(C_L^* - C_0))$ as the vertical coordinate, and the slope is k_La. During the whole experiment, the liquid temperature was detected and maintained within 20 ± 1 °C at all times.

2.5. Experimental Uncertainty. The uncertainties measured at 95% confidence were 0.03, 2.1, 1.7, and 1% for density, viscosity, surface tension, and DOC, respectively.

The uncertainties of bubble velocity and diameter in this study came mainly from the digital image processing. The bubble velocity was determined by dividing the change in bubble center coordinates in two consecutive pictures by the time difference between the two pictures. The uncertainty was expressed as follows:

$$\Delta U = \sqrt{\left(\frac{\partial U}{\partial P_1}\mathrm{d}P_1\right)^2 + \left(\frac{\partial U}{\partial P_2}\mathrm{d}P_2\right)^2 + \left(\frac{\partial U}{\partial \Delta t}\mathrm{d}\Delta t\right)^2 + \left(\frac{\partial U}{\partial S}\mathrm{d}S\right)^2} \tag{11}$$

being $\frac{\partial U}{\partial P_1} = -\frac{S}{\Delta t}$; $\frac{\partial U}{\partial P_2} = \frac{S}{\Delta t}$; $\frac{\partial U}{\partial \Delta t} = \frac{P_2 S - P_1 S}{\Delta t^2}$; $\frac{\partial U}{\partial S} = \frac{P_2 - P_1}{\Delta t}$.

P_1 and P_2 are the bubble center coordinates (pixel), Δt is the time difference between two consecutive images (s), and S is the conversion factor (mm/pixel).

Regarding the bubble velocity (between consecutive images), there are

- Δt =1/fps (=0.002 s, fps = 500); $\mathrm{d}\Delta t = \pm 10^{-6}$ s,
- $\mathrm{d}P_1 = \mathrm{d}P_2 = \pm$ 0.5 pixel. It is due to the fact that the bubble center coordinates may be shifted by around 0.5 pixels during the digital image processing because of losing a line of boundary pixels when the edge detection process took place.
- $\mathrm{d}S$ = 0.00317 mm/pixel. A calibration of 20 cm was used as a reference condition, and the measurement was repeated several times.

The relative measurement error of the bubble velocity is given by $\frac{\Delta U}{U} \times 100\%$. The bubble velocity uncertainty is in the range of 3.58 to 5.84% in S1, 3.55 to 5.73% in S2, 3.42 to 5.91% in S3, 3.37 to 5.87% in S4, and 3.34 to 5.63% in S5.

The uncertainty of the bubble diameter mainly originated from the threshold value set in the digital image processing. It is considered that ±1 pixel is the maximum error of the bubble edge. Uncertainty in the bubble diameter was from 1.90 to 3.84% in S1, from 1.90 to 3.42% in S2, from 1.85 to 3.17% in S3, from 1.86 to 3.51% in S4, and from 1.57 to 3.39% in S5.

3. RESULTS AND DISCUSSION

3.1. Bubbly Flow Regimes. The variation of the gas flow rate (Q_G) leads to different interactions between bubbles and results in differences in the bubbly flow regimes. The bubbly flow regimes of coaxial bubbles are exhibited here. Figure 3 shows bubbly flow regimes at different Q_G in quiescent liquid. Here, the five bubbly flow regimes can be divided into periodic bubbling (single bubbling, bubbling with pairing, and bubbling in groups) and non-periodic bubbling (chaining and jetting). These bubbling regimes found by adjusting Q_G are the same as those proposed by Badam et al.[32] and Wang et al.[33] in water.

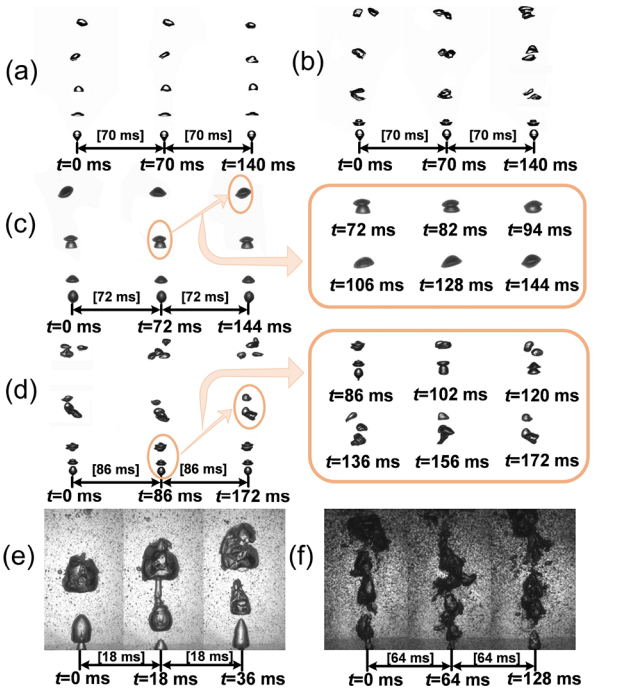

Figure 3. Different bubbly flow regimes in quiescent liquid, with nozzle D = 1.0 mm. (a) Single bubbling (S1 solution, Q_G = 25 mL/min). (b) Bubbling with pairing (S2 solution, Q_G = 95 mL/min). (c) Bubbling with pairing (S5 solution, Q_G = 95 mL/min). (d) Bubbling in groups (S3 solution, Q_G = 110 mL/min). (e) Chaining (S4 solution, Q_G = 1 L/min). (f) Jetting (S1 solution, Q_G = 2 L/min).

At low Q_G, bubbles generate individually at the nozzle in a periodic and regular manner and are not affected by the interactions of neighboring bubbles as shown in Figure 3a, which is called single bubbling. The bubble generation size and period are the same at a constant gas flow rate. With increasing Q_G, the bubble generation size gradually increases and the generation period gradually decreases. The interaction between the neighboring bubbles is enhanced as Q_G increases. After the previous bubble generates and separates from the nozzle, its wake leads to the accelerated formation of the next bubble. After the next bubble separates from the nozzle, it catches up

https://doi.org/10.1021/acsomega.3c01526
ACS Omega 2023, 8, 17159−17170

with the previous one and they rise together in a coalesced or not coalesced pair, as presented in Figure 3b,c, and it is called bubbling with pairing. With further increase in Q_G, the higher Q_G will promote more bubble rise in a group, such as a group of four bubbles rising together as shown in Figure 3d, and this bubbly flow regime is called bubbling in groups. For higher Q_G, after the previous bubble generates and quickly separates from the nozzle, the next bubble is impacted by its wake and forms an elongated bubble. The next bubble rises rapidly and penetrates the previous one, and then they coalesce and break up. During this process, the bubbles rise in a chain and numerous smaller satellite bubbles are generated around them, as illustrated in Figure 3e. This bubbly flow regime is called chaining. When Q_G is high enough, a successive gas flow is jetted from the nozzle, which results in a jet regime, as seen in Figure 3f, and it is called jetting. In this regime, the bubbles continuously undergo coalescence and break up on account of the strong trailing effect. Moreover, numerous small bubbles are generated and dispersed inside the liquid, which prevents the observation of the internal motion of the jetting regime.

A special situation to note about this bubbly flow regime is that most bubble pairs in S1−S4 solutions rise together in a not coalesced pair, and they rise in a particular motion in which they periodically approach and move away from each other (Figure 3b), while only a few bubble pairs occasionally rise together in a coalesced pair. However, in the S5 solution, the bubble pairs rise together only in a coalesced pair (Figure 3c). This is probably because bubbles are more easily coalesced as the liquid viscosity increases.[34] As the liquid viscosity increases, the pair of bubbles changes from a not coalesced to a coalesced pair in the regime of bubbling with pairing.

Table 2 shows bubbly flow regimes at different gas flow rates in different solutions. We notice that the gas flow rate and physical properties of liquid have an essential role in controlling the bubbly flow regime. As Q_G increases, the bubble motion becomes more intense. Bubbling flow regimes are not consistent in solutions with different viscosities.

3.2. Bubble Formation Process. In the periodic bubbling described above, a single bubble can always generate from the nozzle. The bubble formation can be classified into three phases: the waiting phase, the expansion phase, and the detachment phase. The beginning of the bubble evolution is recorded at the moment when the surface of the bubble just sticks out of the nozzle, which is identified as the initial bubble growth moment of this bubble. T_d is the total time from the initial bubble growth moment to the moment of the bubble leaving the nozzle, called the departure time. To better analyze the evolution of bubble formation, we plotted Figure 4, which exhibits the bubble formation evolution at different Q_G. It is obvious that the bubble generation size increases and T_d of the bubble decreases with the increase of Q_G. This indicates that Q_G affects the expansion and detachment phases of the bubbles. The increased Q_G results in a larger momentum of the bubbles being generated and allows them to more quickly achieve the buoyancy that they need to rise. Therefore, as Q_G increases, T_d of the bubble gradually decreases and the bubble generation size becomes larger.

Figure 5 shows the bubble formation evolution in different concentrations of CPRS from the beginning of the expansion phase to the moment of detachment at a 4 mm nozzle and Q_G of 75 mL/min. It is observed that the bubble surface grows slowly above the nozzle after the previous bubble is detached. In S1 solution, the bubble takes the longest time to depart from the nozzle. T_d of the bubble shortens as the concentration of CPRS increases. From Table 1, the liquid viscosity continues to increase as the CPRS concentration increases. We think that the increase of liquid viscosity accelerates the bubble formation process and makes T_d of the bubble gradually shorten. Because T_d of the bubble is shortened, the bubble generation size is gradually smaller under the same condition of nozzle inner diameter and Q_G.

Figure 6 illustrates the evolution of bubble formation in the S2 solution from the beginning of the expansion phase to the moment of detachment at the Q_G of 85 mL/min and different nozzle internal diameters. It is clear that for the nozzle inner diameter of a minimum of 1.0 mm, T_d of the bubble is the shortest and the bubble size formed is the smallest under the same conditions. For the nozzle inner diameter of a maximum of 4.0 mm, T_d of the bubble is the longest and the bubble size is the largest. At the same Q_G, the bubble takes longer to

Table 2. Bubbly Flow Regimes at Different Gas Flow Rates in Different Solutions

gas flow rate (mL/min)	D		
	1.0 mm	2.5 mm	4.0 mm
	S1		
50	bubbling with pairing	single bubbling	single bubbling
150	bubbling in groups	bubbling with pairing	bubbling with pairing
300	chaining	bubbling in groups	bubbling in groups
1000	chaining	chaining	chaining
2000	jetting	jetting	chaining
	S2		
50	single bubbling	single bubbling	single bubbling
150	bubbling in groups	bubbling with pairing	bubbling with pairing
300	bubbling in groups	bubbling in groups	bubbling in groups
1000	chaining	chaining	chaining
2000	jetting	chaining	chaining
	S3		
50	single bubbling	single bubbling	single bubbling
150	bubbling in groups	bubbling with pairing	bubbling with pairing
300	bubbling in groups	bubbling in groups	bubbling in groups
1000	chaining	chaining	chaining
2000	jetting	chaining	chaining
	S4		
50	single bubbling	single bubbling	single bubbling
150	bubbling in groups	bubbling with pairing	bubbling with pairing
300	bubbling in groups	bubbling in groups	bubbling in groups
1000	chaining	chaining	chaining
2000	jetting	chaining	chaining
	S5		
50	single bubbling	single bubbling	single bubbling
150	bubbling in groups	bubbling with pairing	bubbling with pairing
300	bubbling in groups	bubbling with pairing	bubbling with pairing
1000	chaining	chaining	bubbling with pairing
2000	chaining	chaining	chaining

https://doi.org/10.1021/acsomega.3c01526
ACS Omega 2023, 8, 17159−17170

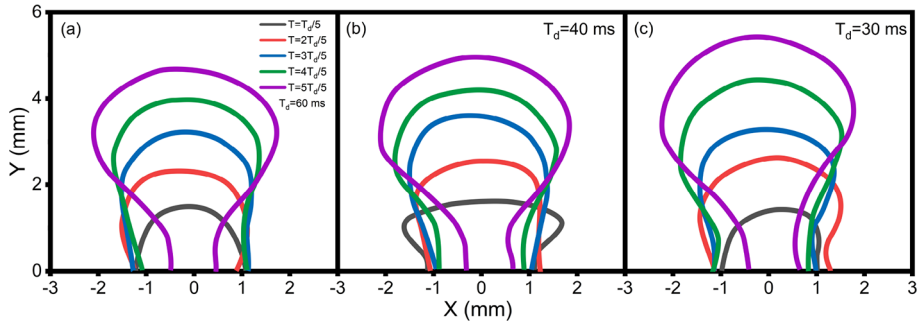

Figure 4. The bubble formation evolution from the beginning of the expansion phase to the moment of detachment in S3 solution at the 2.5 mm nozzle and different Q_G. Q_G is 25 mL/min in (a), 55 mL/min in (b), and 85 mL/min in (c).

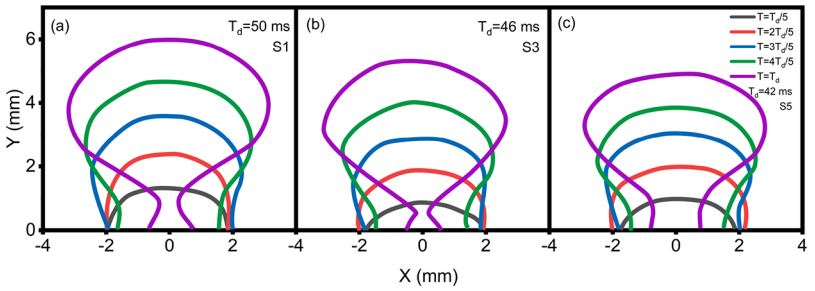

Figure 5. The bubble formation evolution from the beginning of the expansion phase to the moment of detachment in different solutions at the 4 mm nozzle and Q_G of 75 mL/min. The solution is S1 in (a), S3 in (b), and S5 in (c).

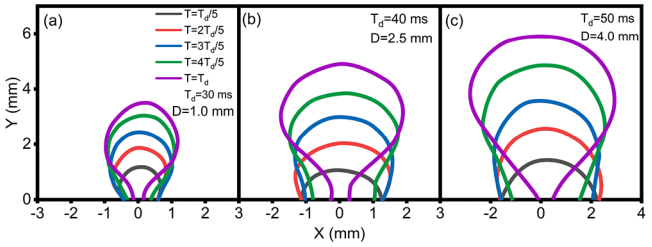

Figure 6. The bubble formation evolution from the beginning of the expansion phase to the moment of detachment in S2 solution at the Q_G of 85 mL/min and different nozzle inner diameters. The nozzle inner diameter is 1.0 mm in (a), 2.5 mm in (b), and 4.0 mm in (c).

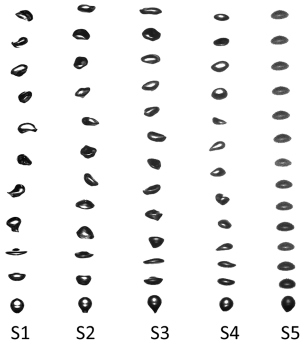

Figure 7. The images of bubbles rising in different solutions (d_e = 4.0 mm, Δt = 0.02 s).

detach as the nozzle inner diameter increases, so the bubble generation size is larger. The larger nozzle inner diameter is one of the reasons for the formation of larger bubbles.

3.3. Dynamic Behaviors of Rising Bubbles. *3.3.1. Single Bubbling.* After the bubble separates from the submerged nozzle, the buoyancy force enables it to rise in the liquid. Figure 7 depicts the rising motion of 4.0 mm bubble in different solutions. As the concentration of CPRS increases, the bubble trajectory gradually tends to be straight and its shape becomes more stable.

Figure 8 depicts the rising velocity of the 4.0 mm bubble with the rising height in different solutions. In Figure 8, the bubble rising velocity in different solutions appears to have distinctive characteristics. When the bubble rises to a height of 60 mm, the bubble velocity reaches a stable final velocity. With the increase of liquid viscosity, the final velocity of the bubbles gradually decreases during the ascent. Figure 9 illustrates the velocity of bubbles with different sizes in S5 solutions. The bubble has the slowest rising velocity when the bubble size is 3.6 mm, and it has the fastest rising velocity when its size is 5.2

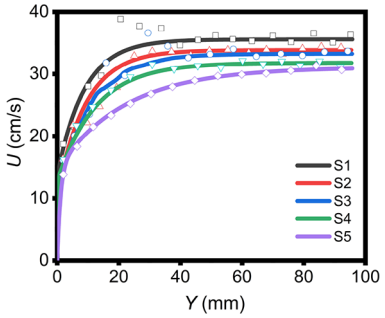

Figure 8. The velocity of the 4.0 mm bubble with the rising height in different solutions.

mm. This shows that the bubble rising velocity increases with increasing bubble size.

In the rising process of the bubble, it is mainly controlled by the buoyancy (F_g) and total resistance forces ($F_{TD} = F_D + F_A + F_B$, F_{TD} is the total resistance forces, F_D is the drag force, F_A is the additional mass force, and F_B is the Basset force), and these

https://doi.org/10.1021/acsomega.3c01526
ACS Omega 2023, 8, 17159−17170

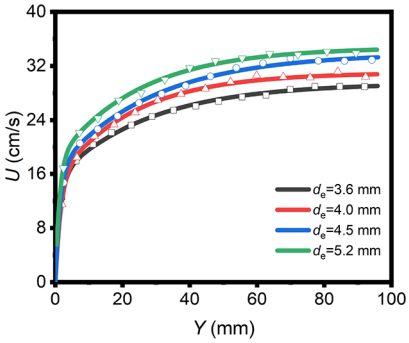

Figure 9. The velocity of bubbles with different sizes in S5 solutions.

forces play an important role in the bubble velocity. Based on these forces that are balanced, the force balance equation can be expressed as follows:

$$m_b\frac{dU}{dt} = F_g + F_D + F_P + F_A + F_B \tag{12}$$

$$C_D = \frac{F_{TD}}{\frac{1}{2}\rho_l U^2\left(\frac{1}{4}\pi d_e^2\right)} = \frac{F_D + F_A + F_B}{\frac{1}{2}\rho_l U^2\left(\frac{1}{4}\pi d_e^2\right)} = \frac{4}{3}d_e\frac{(\rho_l - \rho_g)g - \rho_g\frac{dU}{dt}}{\rho_l U^2} \tag{13}$$

in which m_b represents the bubble weight, F_P is the pressure gradient caused by the external ambient pressure, C_D is the drag coefficient, U is the bubble velocity, ρ_g is the gas density, and ρ_l is the liquid density. Since the density of the experimental liquid is far larger than that of air, the density of air can in eq 12 be overlooked. Moreover, the inertial force is much weaker than F_g.[35] Equation 13 is simplified as follows:

$$C_D = \frac{4d_e g}{3U^2} \tag{14}$$

m_b, F_g, F_D, F_A, F_B, and F_P is calculated as follows:

$$m_b = \frac{1}{6}\pi d_e^3\rho_g \tag{15}$$

$$F_g = \frac{1}{6}\pi d_e^3(\rho_l - \rho_g)g \tag{16}$$

$$F_D = -\frac{1}{2}\rho_l C_D\frac{\pi}{4}d_e^2U^2 \tag{17}$$

$$F_A = -\frac{1}{12}\pi\rho_l d_e^3\frac{d(U_L - U)}{dt} \tag{18}$$

$$F_B = -d_e^2\sqrt{\pi\rho_l\mu_l}\int_{t_0}^{t}\frac{d(U_L - U)/d\tau}{\sqrt{t-\tau}}d\tau \tag{19}$$

$$F_P = -\frac{\pi}{6}d^3\nabla P \tag{20}$$

Here, U_L is the liquid flow rate and μ_l is the liquid viscosity. Minus (−) means force direction, the force in the positive direction is buoyancy, and the downward forces are drag force, additional mass force, and Basset force.

In all experiments, the experimental liquid is quiescent and the liquid height is constant, thus $U_L = 0$. Therefore, it is assumed that the bubble volume is constant in its rising motion. In the single bubble motion, it is situated in a far wake region of the previous one, so it is regarded as $dU_L/dt = 0$, and F_P is negligible, i.e., $\nabla P \approx 0$. F_A and F_B can be simplified as follows:

$$F_A = -\frac{\pi}{12}d_e^3\rho\frac{dU}{dt} \tag{21}$$

$$F_B = -d_e^2\sqrt{\pi\rho_l\mu_l}\int_{t_0}^{t}\frac{dU/d\tau}{\sqrt{t-\tau}}d\tau \tag{22}$$

Figure 10 shows the bubble velocity, force analysis, and drag coefficient. In the bubble motion, F_A and F_B decrease

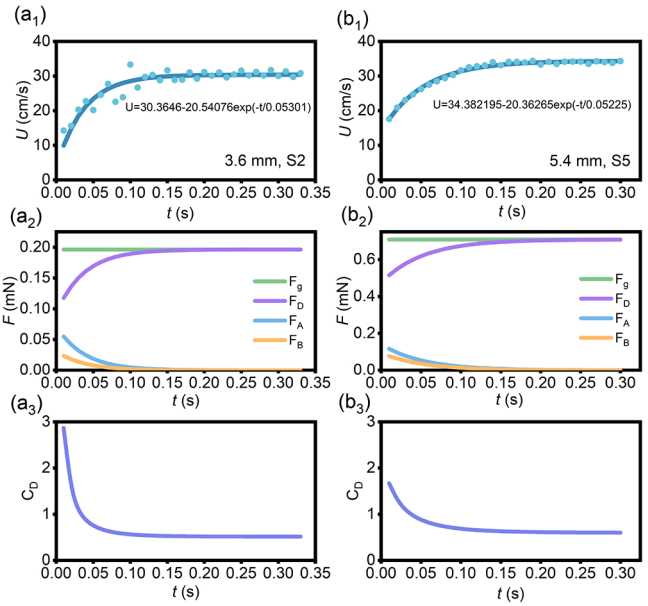

Figure 10. The bubble velocity, force analysis, and drag coefficient. (a_1) 3.6 mm bubble velocity in S2 solution. (a_2) Various forces on the 3.6 mm bubble. (a_3) Drag coefficient of the 3.6 mm bubble. (b_1) 5.4 mm bubble velocity in S5 solution. (b_2) Various forces on the 5.4 mm bubble. (b_3) Drag coefficient of the 5.4 mm bubble.

continuously and tend to 0. Before the bubble reaches the final velocity, F_A and F_B exert a large force on the bubble, which indicates that these two forces play a crucial role in the bubble motion and should not be neglected in the calculation. C_D gradually decreases during the bubble rising, and the F_D of the bubble gradually increases and its value is almost equal to F_g after the bubble reaches the final velocity.

All of the models listed in Table 3 are in a steady motion. The models on petroleum-based liquids, especially CPRS, are few reported in the survey. Figure 11 demonstrates the comparison of C_D predicted by models (1), (2), (3), and (4) with the experimental data. Most of the predicted values in model (1) are obviously much higher than the experimental values. The predicted values in model (4) are either higher or lower than the experimental values. Models (2) and (3) underestimate the experimental values for $Re < 300$. When $Re > 300$, they predict the experimental values poorly in S1 solution but predict accurately in S2−S5 solutions.

These models cannot predict C_D in CPRS well. Therefore, a new correlation is required to predict C_D that is suitable for petroleum-based liquids. However, in the models of Zhang et al.,[36] Karamanev and Nikolov,[20] and Sun et al.,[23] the relation

https://doi.org/10.1021/acsomega.3c01526
ACS Omega 2023, 8, 17159−17170

Table 3. Correlations for Bubble Drag Coefficient

model	reference	correlations	notes
(1)	Zhang et al.[36]	$C_D = ((Re^{0.036} - 0.94)We^{0.43Re^{0.25}} + 1) \times \frac{16}{Re}\left(1 + \left(\frac{8}{Re} + \frac{1}{2}(1 + 3.315Re^{-1/2})\right)^{-1}\right)$	$\begin{cases} 1 \le Re \le 1000 \\ 0 \le We \le 20 \end{cases}$
(2)	Sun et al.[23]	$C_D = \begin{cases} 1.12 \times \frac{24}{Re}(1 + 0.173Re^{0.675}) \\ 0.813 \times \frac{24}{Re}(1 + 24Re^{-1.125}) \\ 1.07 \times \frac{24}{Re^{0.825}}(-1 + 0.037Re^{0.825}) \end{cases}$	$\begin{cases} Re < 10 \\ 10 < Re < 100 \\ 100 < Re \end{cases}$
(3)	Karamanev and Nikolov[20]	$C_D = \begin{cases} 24(1 + 0.173Re^{0.657})Re + \frac{0.143}{(1 + 16300Re^{-1.09})} \\ 0.95 \end{cases}$	$\begin{cases} Re < 130 \\ Re > 130 \end{cases}$
(4)	Cai et al.[21]	$C_D = \begin{cases} 33Re^{-0.94}Mo^{0.03} \\ 3.3 \times 10^{-6}Re^{2}Mo^{0.03} \end{cases}$	$\begin{cases} Re < 350 \\ 350 < Re < 1200 \end{cases}$

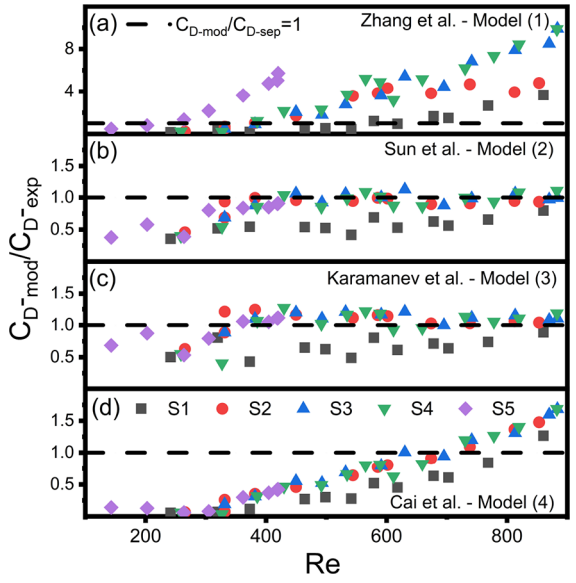

Figure 11. (a) The experimental measured $C_{D\text{-exp}}$ versus the calculated $C_{D\text{-mod}}$ by model (1). (b) The experimental measured $C_{D\text{-exp}}$ versus the calculated $C_{D\text{-mod}}$ by model (2). (c) The experimental measured $C_{D\text{-exp}}$ versus the calculated $C_{D\text{-mod}}$ by model (3). (d) The experimental measured $C_{D\text{-exp}}$ versus the calculated $C_{D\text{-mod}}$ by model (4).

between Re and We is complex and inconvenient. The bubble formation and rising motion process affected by the viscous force and surface tension is significant; thus, we introduce We based on Cai et al.[21] By using a nonlinear fit to the experimental data, we obtain a new correlation for calculating the drag coefficient in CPRS, which is shown in eq 23.

$$C_D = 0.448Re^{4.821}We^{-3.265}Mo^{1.190} \quad (23)$$

Figure 12 presents the comparison of C_D predicted by eq 23 with the experimental data. The C_D predicted by eq 23 is in good agreement with the experimental measured C_D, and the average error is 8.27%.

3.3.2. Bubbling with Pairing. Figure 13 describes the velocity of bubble pairs. During the proximity of these two bubbles to each other, the trailing bubble elongates in its vertical direction and transforms into a bullet shape. The leading bubble is deformed in the horizontal direction and becomes a spherical cap because of the collision. After the pair of bubbles collide, they will rise together as a group or coalesce

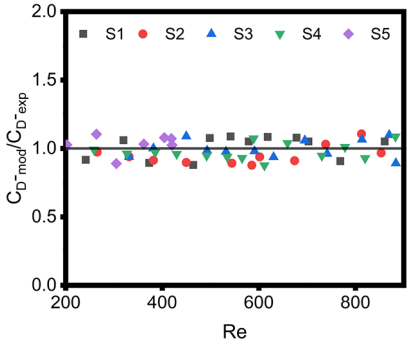

Figure 12. The experimental measured $C_{D\text{-exp}}$ versus the calculated $C_{D\text{-mod}}$ by eq 23.

into a large one. The velocity of the trailing bubble increases until it collides with the leading one. After they collide, the trailing bubble starts to decelerate. When the bubbles rise together as a group, they rise together at a similar velocity. If they coalesce into a large bubble, it will move in a steady manner as an individual bubble. Because the bubbles have more stable velocities in the S5 solution, the bubbles in S5 solution are taken as an example to analyze the forces (F_g, F_A, F_B, and F_D) before collision, as shown in Figure 14. Before they collide, the forces on the leading bubble are close to equilibrium. The leading bubble can be regarded as a single bubble without the influence of the trailing bubble. The F_A that acts as the trailing bubble increases as the distance between the two bubbles shortens, while the F_D gradually decreases. The reason for this is that as the distance between the bubbles shortens and the interactions between the bubbles increases.[37]

3.4. Oxygen Mass Transfer. The changes of dissolved oxygen and volumetric mass transfer coefficients of coaxial bubbles were investigated under different experimental conditions. The experiments were performed in S4 solution with the nozzle inner diameter of 2.5 mm kept constant; the dissolved oxygen and k_La with time at different gas flow rates are shown in Figure 15. k_La increases with increasing Q_G, while the time taken for the liquid to reach oxygen saturation decreases. This may be attributed to bubble generation size and bubble rise velocity increase with increasing gas flow rate, as shown in Figure 4. The high gas flow rate enhances fluid flow near the gas−liquid interface, and gas−liquid mass transfer is intense.

https://doi.org/10.1021/acsomega.3c01526
ACS Omega 2023, 8, 17159−17170

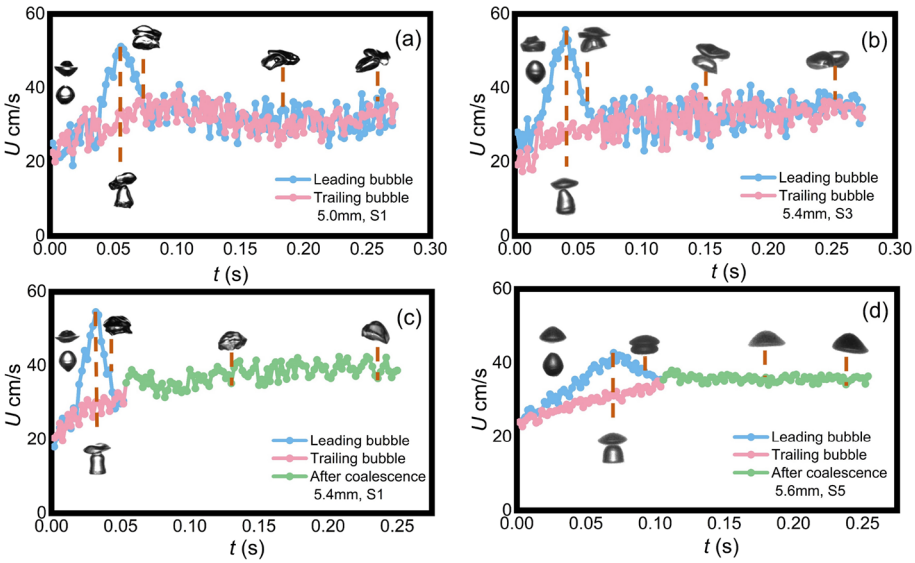

Figure 13. The velocity of bubble pairs. (a) Velocity of 5.0 mm bubble pair without coalescence in S1 solution. (b) Velocity of 5.4 mm bubble pair without coalescence in S3 solution. (c) Velocity of 5.4 mm bubble pair with coalescence in S1 solution. (d) Velocity of 5.6 mm bubble pair with coalescence in S5 solution.

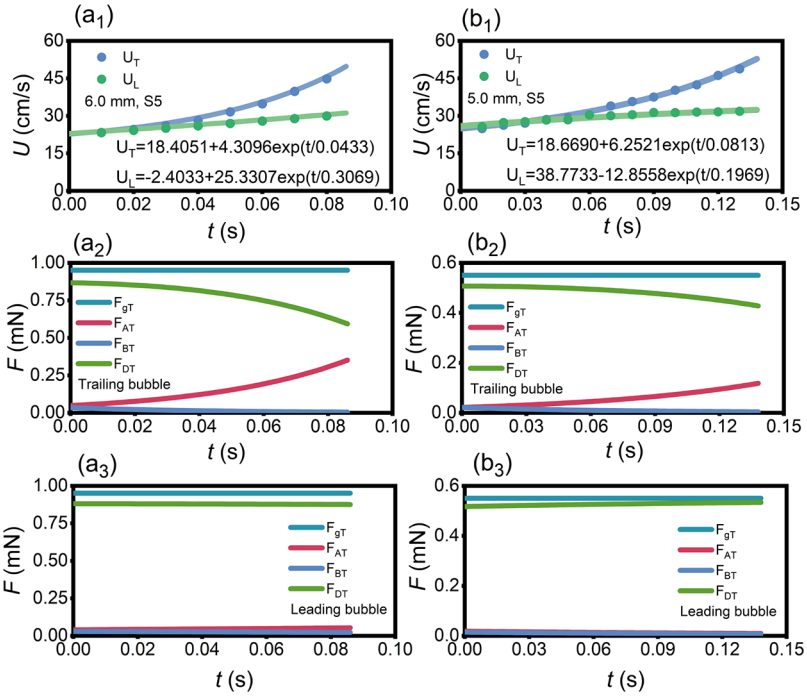

Figure 14. Velocity and forces of bubbles before collide. (a_1) Velocity of 6.0 mm bubble pairs in S6 solution. (a_2) Various forces on the 6.0 mm trailing bubble. (a_3) Various forces on the 6.0 mm leading bubble. (b_1) Velocity of 5.0 mm bubble pairs in S5 solution. (b_2) Various forces on the 5.0 mm trailing bubble. (b_3) Various forces on the 5.0 mm leading bubble.

Figure 16 presents the variation of dissolved oxygen and k_La with time at different nozzle inner diameters. At the same gas flow rate, the time for the liquid to reach oxygen saturation increases with the nozzle inner diameter, while k_La decreases with it. It is probably because at the same gas flow rate, the increase of the nozzle inner diameter leads to a longer bubble detachment time and an increase in the bubble generation size, as shown in Figure 6. During the bubble rising motion, more oxygen accumulates inside the bubble and is stagnant inside the bubble without diffusing into the liquid phase.

The variation of dissolved oxygen and k_La in different solutions is illustrated in Figure 17. As the concentration of CPRS increases, the liquid takes longer to reach oxygen saturation and has a lower k_La. The reason for this is maybe that the liquid viscosity increases as the concentration of CPRS increases. The elevated liquid viscosity will impede gas−liquid mass transfer and promote bubble coalescence,[34,38] which reduces the gas−liquid contact area and results in the decrease of k_La.

https://doi.org/10.1021/acsomega.3c01526
ACS Omega 2023, 8, 17159−17170

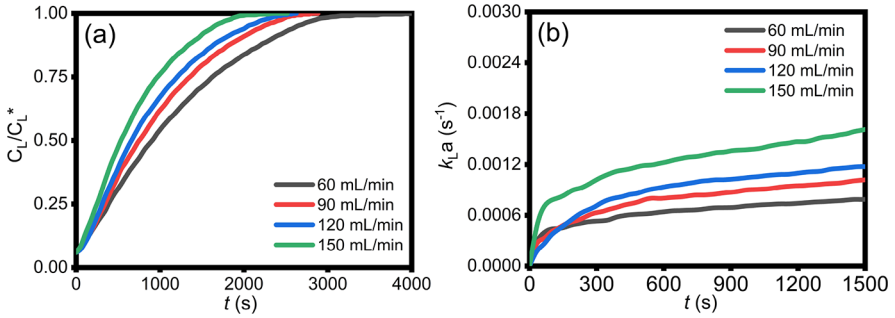

Figure 15. (a) The variation of dissolved oxygen with time at different gas flow rates (S4 solution, D = 2.5 mm). (b) The variation of k_La with time at different gas flow rates (S4 solution, D = 2.5 mm).

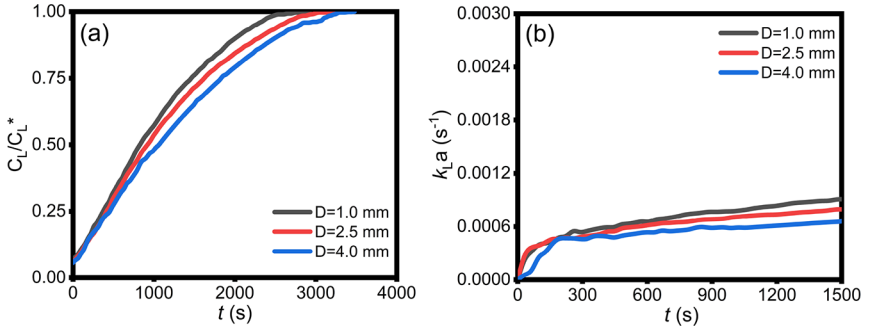

Figure 16. (a) The variation of dissolved oxygen with time at different nozzle inner diameters (S3 solution, Q_G = 120 mL/min). (b) The variation of k_La with time at different nozzle inner diameters (S3 solution, Q_G = 120 mL/min).

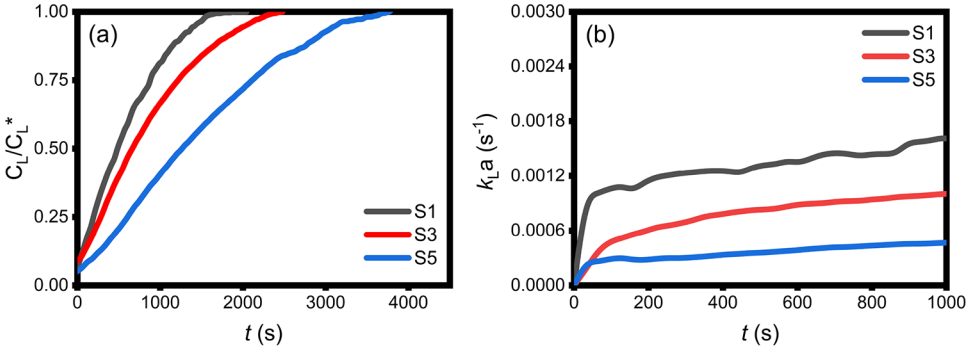

Figure 17. (a) The variation of dissolved oxygen with time in different solutions (D = 4.0 mm, Q_G = 95 mL/min). (b) The variation of k_La with time in different solutions (D = 4.0 mm, Q_G = 95 mL/min).

4. CONCLUSIONS

Herein, the bubble dynamics and mass transfer characteristics of coaxial bubbles in petroleum-based liquids were investigated. The bubble formation process, bubbly flow regime, bubble rising dynamics, and mass transfer characteristics were discussed. The following conclusions can be obtained:

(1) The transition of the bubbly flow regime is influenced by the gas flow rate and the physical properties of the liquid. As the gas flow rate increases, the bubbly flow regime changes. Bubbling flow regimes are not consistent in solutions with different viscosities. The pair of bubbles changes from a not coalesced to a coalesced pair in the regime of bubbling with pairing with the increase of liquid viscosity.

(2) It is found that with increasing gas flow rate, the bubble detachment time shortens and its generation size becomes larger. The bubble sizes in different solutions with the same experimental conditions are different. As the liquid viscosity increases, the bubble generation size decreases.

(3) In CPRS, the bubble rising velocity increases with increasing bubble size and decreases with increasing liquid viscosity. The force analysis of the bubbles indicates that F_A and F_B play an important role in the bubble motion and should not be neglected in the calculation. A new correlation is presented for the drag coefficient applicable to the individual bubbles rising in petroleum-based liquids.

(4) In different experimental conditions, it is discovered that the increase of gas flow rate or nozzle inner diameter can promote mass transfer, while the increase of liquid viscosity can hinder the mass transfer.

https://doi.org/10.1021/acsomega.3c01526
ACS Omega 2023, 8, 17159−17170

AUTHOR INFORMATION

Corresponding Author

Linlin Wang − *School of Chemistry and Chemical Engineering, Guangxi Key Laboratory of Petrochemical Resource Processing and Process Intensification Technology, Guangxi University, Nanning 530004, PR China*; Email: wanglinlin1971@sina.com

Authors

Li Mei − *School of Chemistry and Chemical Engineering, Guangxi Key Laboratory of Petrochemical Resource Processing and Process Intensification Technology, Guangxi University, Nanning 530004, PR China*; orcid.org/0009-0009-7578-7999

Xiaopeng Chen − *School of Chemistry and Chemical Engineering, Guangxi Key Laboratory of Petrochemical Resource Processing and Process Intensification Technology, Guangxi University, Nanning 530004, PR China*; orcid.org/0000-0002-7496-3497

Bei Liu − *PetroChina Guangxi Tiandong Petrochemical Co., Ltd., Tiandong 531599, China*

Zhongyao Zhang − *School of Chemistry and Chemical Engineering, Guangxi Key Laboratory of Petrochemical Resource Processing and Process Intensification Technology, Guangxi University, Nanning 530004, PR China*

Tingting Hu − *School of Chemistry and Chemical Engineering, Guangxi Key Laboratory of Petrochemical Resource Processing and Process Intensification Technology, Guangxi University, Nanning 530004, PR China*

Jiezhen Liang − *School of Chemistry and Chemical Engineering, Guangxi Key Laboratory of Petrochemical Resource Processing and Process Intensification Technology, Guangxi University, Nanning 530004, PR China*; orcid.org/0000-0002-0032-7383

Xiaojie Wei − *School of Chemistry and Chemical Engineering, Guangxi Key Laboratory of Petrochemical Resource Processing and Process Intensification Technology, Guangxi University, Nanning 530004, PR China*

Complete contact information is available at: https://pubs.acs.org/10.1021/acsomega.3c01526

Notes

The authors declare no competing financial interest.

ACKNOWLEDGMENTS

This work was supported by the National Natural Science Foundation of China [Grant Nos. 32160349, 21878056] and the Guangxi Key Laboratory of Petrochemical Resource Processing and Process Intensification Technology [Grant No. 2022Z002].

NOMENCLATURE

Δt	time difference between two consecutive frames
C_L^*	oxygen saturation concentration of the liquid
C_L	current oxygen concentration of the liquid
C_0	initial oxygen concentration of the liquid
C_D	drag coefficient
D	nozzle inner diameter
d_e	bubble equivalent diameter
F_A	additional mass force
F_{AL}	additional mass force on the leading bubble
F_{AT}	additional mass force on the trailing bubble
F_B	Basset force
F_{BL}	Basset force on the leading bubble
F_{BT}	Basset force on the trailing bubble
F_D	drag force
F_{DL}	drag force on the leading bubble
F_{DT}	drag force on the trailing bubble
F_g	combined force of gravity and buoyancy
F_{gL}	combined force of gravity and buoyancy on the leading bubble
F_{gT}	combined force of gravity and buoyancy on the trailing bubble
F_P	pressure gradient caused by the external ambient pressure
F_{TD}	total of all resistance forces
k_La	volumetric mass transfer coefficient
m_b	bubble weight
Q_G	gas flow rate
T_d	bubble departure time
U	bubble velocity
U_L	leading bubble velocity
U_T	trailing bubble velocity
V_x	bubble horizontal velocity
V_y	bubble vertical velocity
X_i	horizontal coordinate of the bubble centroid
Y_i	vertical coordinate of the bubble centroid
μ_l	liquid viscosity
ρ_g	gas density
ρ_l	liquid density
σ	surface tension

REFERENCES

(1) Pasaoglu, M. E.; Koyuncu, I. Substitution of petroleum-based polymeric materials used in the electrospinning process with nanocellulose: A review and future outlook. *Chemosphere* **2021**, *269*, No. 128710.

(2) Yu, C.; Huang, H.; Li, Q.; Xu, R.; Tao, S.; Xiao, X.; Luo, Y.; Fang, J. New advances in catalysts for C9 petroleum resin hydrogenation, *IOP Conference Series: Earth and Environmental Science*; IOP Publishing, 2020, *513*(1), 012003.

(3) Zhou, D.; Chen, X.; Liang, J.; Wei, X.; Wu, C.; Li, W.; Wang, L. High-Temperature Stability and Pyrolysis Kinetics and Mechanism of Bio-Based and Petro-Based Resins Using TG−FTIR/MS. *Ind. Eng. Chem. Res.* **2021**, *60*, 13774−13789.

(4) Li, F.; Yang, Y.; Dai, D.; Yuan, Y. Study on the Preparation of the Waterproofing Agent for the Mineral Wool Board by Modified C9 Petroleum Resin. *China Pet. Process. Petrochem. Technol.* **2013**, *15*, 92.

(5) Wu, C.; Chen, X.; Tang, L.; Wei, Q.; Wei, X.; Liang, J.; Wang, L. Rationally constructing A nano MOF-derived Ni and CQD embedded N-doped carbon nanosphere for the hydrogenation of petroleum resin at low temperature. *ACS Appl. Mater. Interfaces* **2021**, *13*, 10855−10869.

(6) Wang, R.; Sun, H.; Liang, M.; Zhang, H.; Cui, Q.; Wang, T.; Yuan, P. Flower-like nickel phosphide catalyst for petroleum resin hydrogenation with enhanced catalytic activity, hydrodesulfurization ability and stability. *Chem. Eng. Sci.* **2022**, *264*, No. 118180.

(7) Wang, D.; Guo, J.; Su, M.; Sun, J.; Zhang, S.; Yang, W.; Gu, X.; Li, H. The application of a novel char source from petroleum refining waste in flame retardant thermoplastic polyurethane. *Polym. Eng. Sci.* **2020**, *60*, 1029−1034.

(8) Kanat, M.; Eren, T. Synthesis of phosphorus-containing flame retardants and investigation of their flame retardant behavior in textile applications. *J. Appl. Polym. Sci.* **2019**, *136*, 47935.

(9) Gumulya, M.; Utikar, R. P.; Evans, G. M.; Joshi, J. B.; Pareek, V. Interaction of bubbles rising inline in quiescent liquid. *Chem. Eng. Sci.* **2017**, *166*, 1−10.

(10) Mohseni, E.; Kalayathine, J. J.; Reinecke, S. F.; Hampel, U. Dynamics of bubble formation at micro-orifices under constant gas flow conditions. *Int. J. Multiphase Flow* **2020**, *132*, No. 103407.
(11) Wang, X.; Song, M.; Li, S.; Huang, Y. Dynamic behaviors of bubble formation on submerged micro-capillary under constant flow conditions. *Powder Technol.* **2023**, *417*, No. 118258.
(12) Xiang, S.; Jian, Z.; Kherbeche, A.; Thoraval, M.-J. Experimental study of single bubble rising near vertical wall in hele-shaw cell. *Chem. Eng. Sci.* **2022**, *255*, No. 117647.
(13) Oshaghi, M. R.; Shahsavari, M.; Afshin, H.; Firoozabadi, B. Experimental investigation of the bubble motion and its ascension in a quiescent viscous liquid. *Exp. Therm. Fluid Sci.* **2019**, *103*, 274−285.
(14) Gómez-Díaz, D.; Navaza, J. M.; Quintáns-Riveiro, L. C.; Sanjurjo, B. Gas absorption in bubble column using a non-Newtonian liquid phase. *Chem. Eng. J.* **2009**, *146*, 16−21.
(15) Shi, H.; Jiang, H.; Liu, Y.; Chen, R. Bubble dynamics and mass transfer characteristics from an immersed orifice plate. *J. Chem. Technol. Biotechnol.* **2020**, *95*, 1729−1738.
(16) Salibindla, A. K. R.; Masuk, A. U. M.; Tan, S.; Ni, R. Lift and drag coefficients of deformable bubbles in intense turbulence determined from bubble rise velocity. *J. Fluid Mech.* **2020**, *894*, A20.
(17) Wang, P.; Cilliers, J. J.; Neethling, S. J.; Brito-Parada, P. R. The behavior of rising bubbles covered by particles. *Chem. Eng. J.* **2019**, *365*, 111−120.
(18) Mach, J.; Wiens, J.; Adjaye, J.; Donaldson, A. A.; Macchi, A. Effect of pressure on the drag coefficient of individual bubbles in a contaminated polydisperse swarm. *Chem. Eng. Sci.* **2020**, *223*, No. 115728.
(19) Yan, X.; Zheng, K.; Jia, Y.; Miao, Z.; Wang, L.; Cao, Y.; Liu, J. Drag Coefficient Prediction of a Single Bubble Rising in Liquids. *Ind. Eng. Chem. Res.* **2018**, *57*, 5385−5393.
(20) Karamanev, D. G.; Nikolov, L. N. Free rising spheres do not obey newton's law for free settling. *AIChE J.* **1992**, *38*, 1843−1846.
(21) Cai, Z.; Bao, Y.; Gao, Z. Hydrodynamic Behavior of a Single Bubble Rising in Viscous Liquids. *Chin. J. Chem. Eng.* **2010**, *18*, 923−930.
(22) Jamialahmadi, M.; Branch, C.; Müller-Steinhagen, H. Terminal bubble rise velocity in liquids. *Chem. Eng. Res. Des.* **1994**, *72*, 119−122.
(23) Sun, B.; Guo, Y.; Wang, Z.; Yang, X.; Gong, P.; Wang, J.; Wang, N. Experimental study on the drag coefficient of single bubbles rising in static non-Newtonian fluids in wellbore. *J. Nat. Gas Sci. Eng.* **2015**, *26*, 867−872.
(24) Tian, Z.; Cheng, Y.; Li, X.; Wang, L. Bubble shape and rising velocity in viscous liquids at high temperature and pressure. *Exp. Therm. Fluid Sci.* **2019**, *102*, 528−538.
(25) Battistella, A.; van Schijndel, S. J. G.; Baltussen, M. W.; Roghair, I.; van Sint Annaland, M. On the terminal velocity of single bubbles rising in non-Newtonian power-law liquids. *J. Non-Newtonian Fluid Mech.* **2020**, *278*, No. 104249.
(26) Kováts, P.; Thévenin, D.; Zähringer, K. Influence of viscosity and surface tension on bubble dynamics and mass transfer in a model bubble column. *Int. J. Multiphase Flow* **2020**, *123*, No. 103174.
(27) Chaumat, H.; Billet, A.-M.; Delmas, H. Hydrodynamics and mass transfer in bubble column: Influence of liquid phase surface tension. *Chem. Eng. Sci.* **2007**, *62*, 7378−7390.
(28) Mehrnia, M. R.; Towfighi, J.; Bonakdarpour, B.; Akbarnejad, M. M. Gas hold-up and oxygen transfer in a draft-tube airlift bioreactor with petroleum-based liquids. *Biochem. Eng. J.* **2005**, *22*, 105−110.
(29) Kowal, M.; Żejmo, M.; Skobel, M.; Korbicz, J.; Monczak, R. Cell Nuclei Segmentation in Cytological Images Using Convolutional Neural Network and Seeded Watershed Algorithm. *J. Digital Imaging* **2020**, *33*, 231−242.
(30) Scargiali, F.; Busciglio, A.; Grisafi, F.; Brucato, A. Simplified dynamic pressure method for measurement in aerated bioreactors. *Biochem. Eng. J.* **2010**, *49*, 165−172.
(31) Lau, R.; Lee, P. H. V.; Chen, T. Mass transfer studies in shallow bubble column reactors. *Chem. Eng. Process.* **2012**, *62*, 18−25.
(32) Badam, V. K.; Buwa, V.; Durst, F. Experimental investigations of regimes of bubble formation on submerged orifices under constant flow condition. *Can. J. Chem. Eng.* **2007**, *85*, 257−267.
(33) Wang, H.; Dong, F.; Song, L. Bubble-forming regime identification based on image textural features and the MCWA feature selection method. *IEEE Access* **2017**, *5*, 15820−15830.
(34) Feng, J.; Li, X.; Bao, Y.; Cai, Z.; Gao, Z. Coalescence and conjunction of two in-line bubbles at low Reynolds numbers. *Chem. Eng. Sci.* **2016**, *141*, 261−270.
(35) Yan, X.; Jia, Y.; Wang, L.; Cao, Y. Drag coefficient fluctuation prediction of a single bubble rising in water. *Chem. Eng. J.* **2017**, *316*, 553−562.
(36) Zhang, L.; Zhou, Z.; Deng, J.; Shao, X. A numerical study on the drag law of a gas bubble using dynamic body force method. *Phys. Fluids* **2021**, *33*, No. 063320.
(37) Schlichting, H., *Boundary-layer theory*; 7th Ed., McGraw-Hill Book Company, New York: 1979.
(38) Song, D.; Seibert, A. F.; Rochelle, G. T. Effect of liquid viscosity on the liquid phase mass transfer coefficient of packing. *Energy Procedia* **2014**, *63*, 1268−1286.

https://doi.org/10.1021/acsomega.3c01526
ACS Omega 2023, 8, 17159−17170